Contents lists available at ScienceDirect

J. Vis. Commun. Image R.

An automated three-dimensional plus time registration framework for dynamic MR renography

Ting Song [a,b,*], Vivian S. Lee [b], Qun Chen [b], Henry Rusinek [b], Andrew F. Laine [a]

[a] Department of Biomedical Engineering, Columbia University, ET-351, 1210 Amsterdam Avenue, New York, NY 10027, USA
[b] Center for Biomedical Imaging, NYU School of Medicine, 660 1st Ave., FL1, New York, NY 10016, USA

ARTICLE INFO

ABSTRACT

Dynamic contrast-enhanced 3D images of the kidneys, or 3D MR renography, has the potential for broad clinical applications, but suffers from respiratory motion that limits analysis and interpretation. Manual registration is prohibitively labor-intensive. In this paper, a fully automated technique, Wavelet Representation and the Fourier Transform (WRFT) method, that corrects for translation and rotation motion in 3D MR renography is presented. The method was composed by anisotropic denoising, wavelet-based feature extraction, and Fourier-based registration. This was first evaluated on a set of simulated MR renography images with defined degrees of kidney motion. The method was then tested on 24 clinical patient MR renography data sets. Results of clinical testing were compared with the results obtained using a mutual information registration method. Based on intrarenal time-intensity curves, our method showed robust and consistent agreement with the results of manually coregistered data sets.

1. Introduction

The kidneys are vital organs that serve to filter out harmful waste products and excess water from the blood. Measurements of kidney function are critical to patient care, with existing tests limited primarily to measurements of global renal function. Single kidney glomerular filtration rate and split renal function can be non-invasively measured by gadolinium-enhanced 3D dynamic MR renography [1]. With 3D dynamic MR renography protocol, 3D images are acquired repeatedly over time after intravenous injection of a low dose of gadolinium, a safe and sensitive contrast agent. Image analysis of these contrast-enhanced images aims to extract and then model time-intensity curves from each functional renal compartment (renal cortex, medulla, and the collecting system). Since patients often cannot reproducibly hold their breath during data acquisition, accurate computation of time-intensity curves requires spatial alignment of images over time to correct for respiratory motion. In an earlier study [1], manual 3D registration and segmentation of all images were performed separately for each kidney by two experienced investigators, requiring approximately 2–3 h at a workstation per case. For clinical applications, this approach is prohibitively time- and labor-intensive. Therefore,

automated image registration techniques to correct respiratory motion are of great clinical interest and importance.

Due to that segmentation is also the base of the registration, a brief introduction of segmentation is presented. The challenging part for dynamic contrast-enhanced image segmentation is that when contrast agent wash-in and wash-out occurs, image intensity values change rapidly as the time series evolves. Of course poor kidney function or stenotic vasculature may prevent the uptake of contrast agent, resulting in disjointed disjoined bright regions. Accurate and continuous boundary delineation is not always feasible. Basically, kidney segmentation techniques can be divided in two basic categories: spatial or temporal. In the spatial approach segmentation is performed separately at each time point [2,3]. Temporal or vector segmentation considers each voxel's intensity time course as a vector and classifies the tissues according their different features and behaviors occurring in the temporal domain [4–7].

There has been limited work related to the registration of dynamic MRI images of the abdominal region. Prior studies were restricted in 2D plus time and in-plane motion only [8]. Two registration methods for minimization of the effects of kidney motion on 2D images have been discussed by [9]. Both methods were semi-automated and required the use to trace contours of the kidney boundaries. Another integrated dynamic renal perfusion MR image registration algorithm was used by [7] to correct for 2D in coronal-plane translation component of respiratory motion. Their study used Sobel edge detection filters to correct for large scale motion.

Registration was then refined based on local gradients and auxiliary 2D image segmentation results. However in this study, rotation and out-of-plane motion were not corrected. Sun et al. applied their method, combined with a 2D subpixel registration algorithm to correct for respiratory motion, to rat renal perfusion MR images [10]. Their 2D method minimized an energy function that integrated a translational motion model and temporal smoothness constraints. Tests with rat kidney transplants showed that the algorithm compensated for the breathing motion and extracted the kidneys, cortex, and pelvis, where translational movement was limited to head-to-feet within one pixel. Gerig et al. put forward a 2D scheme for automatic detection of the kidney contours, extraction of in-plane motion parameters per frame, and registration of 2D images [11]. Boundary features are extracted first, and then the Hough transform served as a model-guided global method of grouping. Finally, the displacement and rotation parameters of the objects were determined by the location and the rotational parameters obtained from the evaluation of correlation maxima. Giele et al. used a 2D phase difference method for kidney image motion correction, which is limited to in-plane registration [12]. Boykov et al. used a mutual information method to correct for the translational displacement among 3D serial renal images, without solving the rotation problem [5]. However, a fully 3D registration method correcting both translation and rotation is still not available.

In this context, we propose a novel, fully automated dynamic 3D MR renography registration framework based on Wavelet Representation and the Fourier Transform (WRFT) expansions. First, a preprocessing step of denoising is employed using edge-preserving anisotropic diffusion; second, edge detection is implemented using a 3D over-complete dyadic wavelet expansion; third, using these edge images, a 3D registration is accomplished using phase information in Fourier space. In the sections below, we show how our method was quantitatively evaluated on a phantom built from clinical data as well as on 24 clinical data sets each compared with manually registered ground truth data. Furthermore, this WRFT framework was also compared with traditional 3D mutual information based registration technique.

2. Methodology

2.1. Overview of processing steps

The WRFT framework was composed by three components: anisotropic denoising, wavelet-based feature extraction, and Fourier-based 3D registration. Given a series of multiple contrast-enhanced 3D renal MR images, 3D anisotropic diffusion was first applied to reduce noise in the acquired image data. Based on these denoised data, a 3D dyadic wavelet representation was applied to extract major edge information and features relevant to the internal structure and compartments of the kidney. Next, these features were fed into a 3D Fourier-based registration method to correct 3D rotation and translation of the kidney due to the respiration.

2.2. Anisotropic diffusion

If edge detection is applied directly to the original serial 3D images, false edges caused by noise prevent the registration process from achieving sufficient accuracy. Therefore, a denoising process is both beneficial and may be necessary for some patient data. Montagnat and Weickert proved that anisotropic diffusion could markedly reduce image noise without over-smoothing edges, and showed that such denoising improves segmentation robustness [13,14]. A Gaussian kernel has a major drawback in that it is difficult to obtain accurately the locations of the strong and useful edges. Anisotropic filtering has the advantage of spatially encouraging intra-region smoothing in preference to inter-region smoothing [15]. Therefore, we have applied a computationally efficient denoising filter based on anisotropic diffusion previously developed by [16] for 3D cardiac ultrasound data analysis.

In general anisotropic diffusion methods [15], apply the following type of dynamic heat diffusion equation to the gray levels of any given 3D plus time image data $I(x, y, z, t)$:

$$\frac{\partial I}{\partial t} = div(c(x, y, z, t)\nabla I), \tag{1}$$

where $c(x, y, z, t)$ is the diffusion parameter, *div* denotes the divergence operator, and ∇I denotes the gradient of the image intensity.

In the original work of [15], the concept of anisotropic diffusion was introduced with the selection of a variable diffusion parameter, a function of the gradient of the data:

$$c(x, y, z, t) = g(|\nabla I(x, y, z, t)|). \tag{2}$$

We used the diffusion function proposed by [17] defined as:

$$g(x, \lambda) = \begin{cases} 1 & x \le 0 \\ 1 - e^{-\frac{3.315}{(x/\lambda)^4}} & x > 0 \end{cases}. \tag{3}$$

Eq. (1) can be numerically solved via explicit or implicit finite difference equations. The parameter λ serves as a gradient threshold, defining edge points x_k as locations where $|\nabla I_{x_k}| > \lambda$. This bell-shaped diffusion function acts as an edge-enhancing filter, with high diffusion values in smooth areas and low values at edge points. The structure of the diffusion tensor with separate weights for each dimension allows control of the direction of the diffusion process, with flows parallel to edge contours.

Diffusion coefficient curves with different gradient threshold values showed that the larger the gradient threshold, the wider the range in which image gradients will be smoothed or weakened. The curve also reduces to zero at about 5λ. The gradient threshold is selected based on the decreased properties of the diffusion coefficient curve.

As the contrast agent washes in, image data properties change, and it becomes necessary to modify the gradient threshold parameter value within each time series of data. In [13] a decrease in the value of significant edges was used as the homogeneous regions in ultrasound data were filtered. They decreased the threshold gradient over time and proposed values based on a fraction of the cumulative histograms of the data gradients recomputed at each iteration of the diffusion process. After experimenting with different strategies for setting the gradient threshold value on our data, we used a linear model where

$$\lambda(t) = \lambda_0 + at, \tag{4}$$

with λ_0 is the initial gradient value, a is a slope parameter and t is the time iteration index. Parameters for the data sets processed as $\lambda_0 = 7$ and $a = -0.02$ with 10 iterations were set empirically. Since all the images are using the same MR protocol (i.e. same acquisition parameters, e.g. TR, TE, etc.) which gave the similar signal to noise ratio, the selection of parameter a is not sensitive across patient's and time frames. The gradient magnitudes of the image features were larger than 35 pixel intensities whereas the gradient magnitudes of noise were within 10 pixel intensities. Therefore, in order to preserve image features, the initial gradient threshold was set to one fifth of the lower bound of feature gradient, 7, with a slightly decreasing slope of −0.02. Sample slices before and after anisotropic diffusion are shown in Fig. 1, from which it can be clearly seen that noise is suppressed, while important image features are preserved.

2.3. Wavelet edge detection

In dynamic MRI tissue contrast varies with time and different compartmental organs of the kidney are enhanced in time after
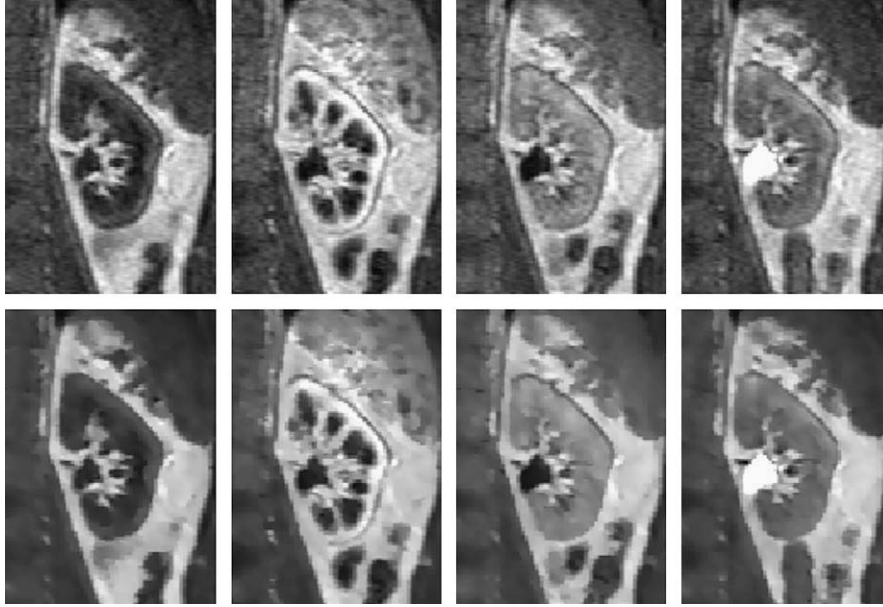
T. Song et al./J. Vis. Commun. Image R. 21 (2010) 1–8

3

Fig. 1. Sample anisotropic diffusion comparison (coronal view): first row contains original images; second row shows diffused images. Columns from left to right are the 1st (pre-contrast), 10th (cortex enhanced), 18th (modulla enhanced), 37th (collecting system enhanced) time frames. Signals within each tissue are visibly smoother and more homogeneous after diffusion.

injection. Variable patterns of enhancement means that intensity image alone are not reliable for organ registration. Instead, we must rely on stable edge information which is preserved well throughout the serial 3D image volumes. One way of implementing a multi-dimensional discrete dyadic transform is to use a filter bank scheme with separable wavelet bases [18]. Since the research in this paper focuses on three-dimensional image processing, we used a three-dimensional discrete dyadic transform. Wavelet bases were constructed as a tensor product of a separable bases function for each dimension. Similar to the 1D case, wavelet bases can be designed as derivatives of spline functions, which are excellent multi-scale edge detectors. A 3D discrete dyadic wavelet transform of M level analysis can be represented as a set of wavelet coefficients

$$\left\{ S_M s(n_1,n_2,n_3), \left\{ W_M^1 s(n_1,n_2,n_3), W_M^2 s(n_1,n_2,n_3), W_M^3 s(n_1,n_2,n_3) \right\} \right\},$$ (5)

where $W_M^k s(n_1,n_2,n_3) = \langle s, \psi_{m,n_1,n_2,n_3}^k \rangle, k = 1,2,3$ are coefficients after high-pass filtering, $S_M s(n_1,n_2,n_3)$ are coefficients after low-pass filtering, and the scale $m = 1, \ldots, M$. The wavelet bases are dilated and translated from wavelet functions:

$$\psi_{m,n_1,n_2,n_3}^k(x,y,z) = \frac{1}{2^{3m/2}} \psi^k \left(\frac{x-n_1}{2^m}, \frac{y-n_2}{2^m}, \frac{z-n_3}{2^m} \right), \quad k = 1,2,3.$$ (6)

Notice that a 3D dyadic wavelet transform consists of three components at each level of expansion. They provide representations of detail information along each of the Cartesian coordinate directions at each expansion level (scale). The wavelet modulus $M_m f$ of a 3D signal f at scale m can then be computed from these individual wavelet coefficients [19,20]:

$$M_m f = \sqrt{|W_m^1 f|^2 + |W_m^2 f|^2 + |W_m^3 f|^2}.$$ (7)

An example of a 3D dyadic over-complete wavelet expansion is shown in Fig. 2. The coarse and detail channels at three distinct levels of analysis are shown with the corresponding extracted edge information. From the plot, it can be seen that wavelet modulus,

or extracted edges, from a 2-level expansion retains the most important compartmental features of the kidney without losing too much detail. Based on this experimental rationale and the matrix size of our raw data, we selected the modulus at level 2 analysis for registration.

Moreover, with over-complete wavelet expansion and zero-phase filters; there is no spatial shift of the position of edges across levels of expansion. This mathematical property of translation invariance is essential under our registration application. This property cannot be achieved by the other methods when combined with regular multi-resolution analysis techniques that may include frequency dependent phase shifts across scales of an expansion.

2.4. Fourier-based registration

Using edge images acquired from the previous step, a 4D registration framework was accomplished by considering the first frame as the reference of a 3D kidney volume; the subsequent 3D frames in time were then registered to the first one. Our work utilizes a 3D motion correction method [21] based on the Fourier transform. One of the benefits of the method is that it makes use of all available information instead of a limited set of features from the images. We will show that this makes the procedure very robust.

The procedure is described as follow. Let $f(x,y,z)$ be a 3D volume data, and let $g(x,y,z)$ be a translated and rotated version of $f(x,y,z)$, then

$$g(x,y,z) = f(R(x,y,z)^T + t),$$ (8)

where $t \in R^3$ is a translation vector, and $R \in SO(3)$ is a rotation matrix.

The 3D Cartesian Fourier transform of $g(x,y,z)$ would be

$$\mathfrak{F}[g](w_x, w_y, w_z) = \int \int \int g(x,y,z) e^{-j2\pi[w_x x + w_y y + w_z z]} dx \, dy \, dz.$$ (9)

To simplify notation, vector representation will be adopted. Let X denote the column vector $(x,y,z)^T$, and let W denote the column vector $(w_x, w_y, w_z)^T$ in frequency domain. Then we can rewrite the Eq. (9) as
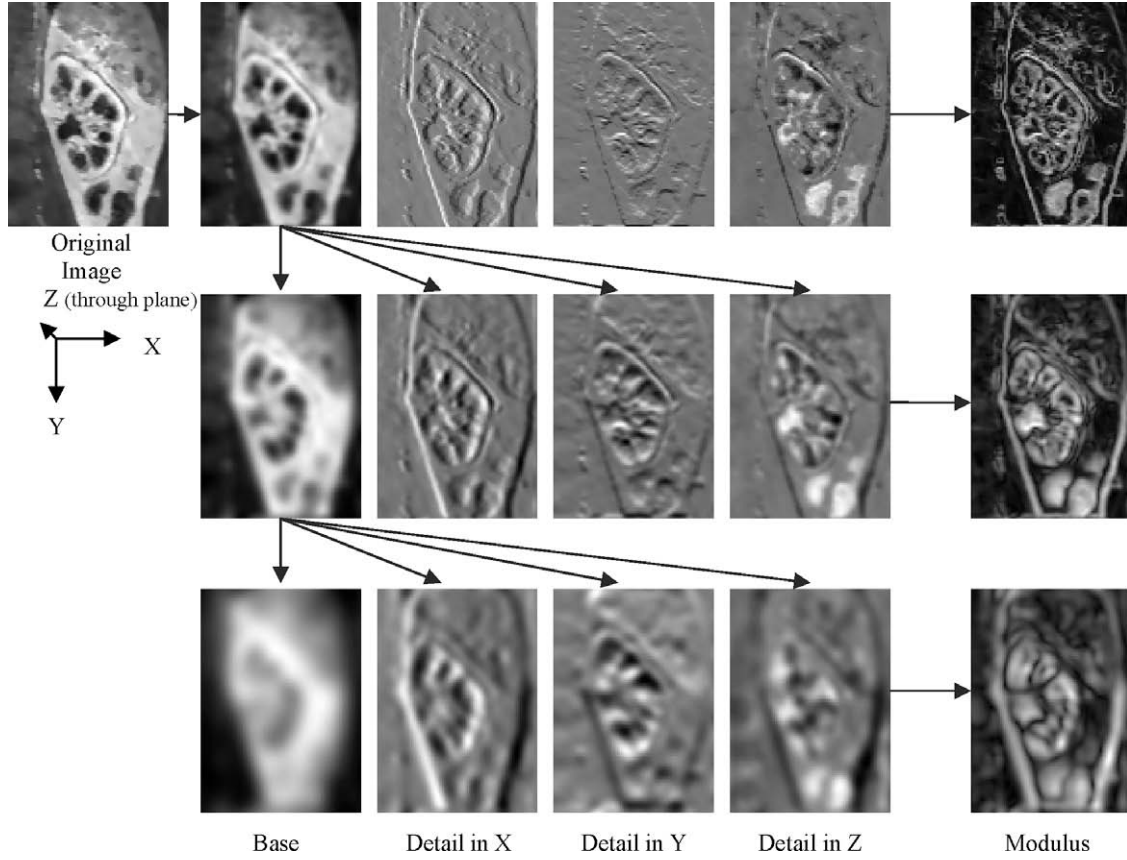
Fig. 2. Illustration of a 3D dyadic over-complete wavelet expansion (levels 1–3, rows 1–3) and corresponding extracted detail and modulus information after anisotropic diffusion as shown in Fig. 1.

$$\mathfrak{F}[g](W) = \int \int \int g(x)e^{-j2\pi W^T X} dX. \tag{10}$$

Then the Fourier transform of g could be expressed in the Fourier transform of f:

$$\mathfrak{F}[g](W) = \int \int \int f(RX + t)^{-j2\pi W^T X} dX. \tag{11}$$

Let $X' = RX + t$, then $X = R^{-1}X' - R^{-1}t$. Since R is a unitary matrix, $R^{-1} = R^T$ and $dX = dX'$.

From the above equations, we can see that the estimation of rotation can be decoupled from the estimation of translation. Thus, the first estimation of R should be implemented before the estimation of t. In 2D space, rotation can be completely expressed by one angle in polar coordinates, in order to represent a rotation. In 3D space, three angles are needed (Euler's rotation theorem to describe rotation). Rodrigues' rotation formula is adopted, which gives an efficient method for computing the rotation matrix $R \in SO(3)$ corresponding to a rotation by an angle $\psi \in \mathbb{R}$ about a rotation axis specified by the unit vector $\tilde{\omega} = (\omega_x, \omega_y, \omega_z) \in \mathbb{R}^3$. Then R is given by

$$R = \begin{bmatrix} \cos\psi + \omega_x^2(1-\cos\psi) & \omega_x\omega_y(1-\cos\psi) - \omega_z\sin\psi & \omega_y\sin\psi + \omega_x\omega_z(1-\cos\psi) \\ \omega_z\sin\psi + \omega_x\omega_y(1-\cos\psi) & \cos\psi + \omega_y^2(1-\cos\psi) & -\omega_x\sin\psi + \omega_y\omega_z(1-\cos\psi) \\ -\omega_y\sin\psi + \omega_x\omega_z(1-\cos\psi) & \omega_x\sin\psi + \omega_y\omega_z(1-\cos\psi) & \cos\psi + \omega_z^2(1-\cos\psi) \end{bmatrix}_{3\times3}. \tag{14}$$

$$\mathfrak{F}[g](W) = \int \int \int f(X')e^{-j2\pi W^T(R^{-1}X' - R^{-1}t)} dX'$$
$$= \int \int \int f(X')e^{-j2\pi (RW)^T X'} e^{j2\pi (RW)^T t} dX'$$
$$= \mathfrak{F}[f](RW)e^{j2\pi (RW)^T t} \tag{12}$$

Moreover, we can get

$$|\mathfrak{F}[g](W)| = |\mathfrak{F}[f](RW)|. \tag{13}$$

Since any unit vector in 3D space can be expressed by two angles (θ, ϕ), the rotation axis unit vector can be calculated by three angles (θ, ϕ, ψ):

$$\omega_x = \cos\theta\cos\phi, \quad \omega_y = \sin\theta\cos\phi, \quad \omega_z = \sin\phi. \tag{15}$$

From a 3D phantom (a Gaussian ellipsoid) example, rotation and translation corrections are next demonstrated. A homogeneous 3D image g was generated by rotating image f with rotation parameters: [0 90 9] degrees. Both images have dimensions of [32 32 32]. After correction, the results showed rotation parameter: [0 89.98 8.97].
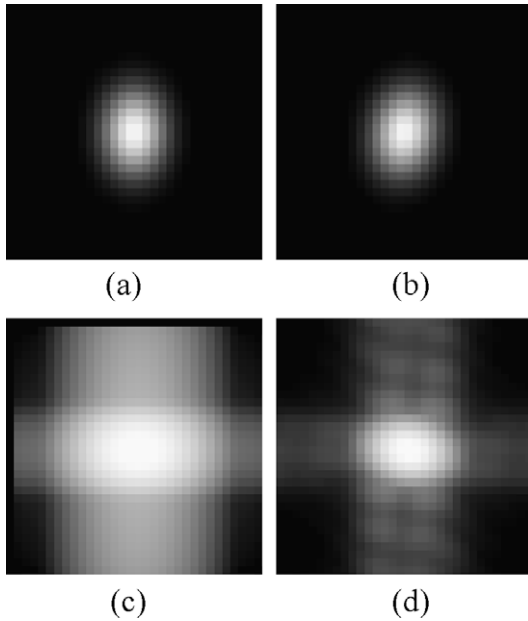
Fig. 3. Illustration of rotation effects on magnitude spectrum. A homogeneous 3D image g was generated by rotating image f with rotation parameters: [0 90 9] degrees. Both images have dimensions of [32 32 32]. (a) and (b) are the 16th slice in XY plane of images f and g; (c) and (d) are the 16th slice of magnitude spectrums in $\omega_x\omega_y$ plane corresponding to images f and g.

From Fig. 3, we can see that the rotation of the magnitude spectrum represents the original image rotation.

Similarly, translation in the spatial domain will introduce a phase shift in spectrum. In the phase domain, as illustration in the example, Fig. 4, translation with parameters [0 −2 0] was corrected by exactly the same parameters of the algorithm.
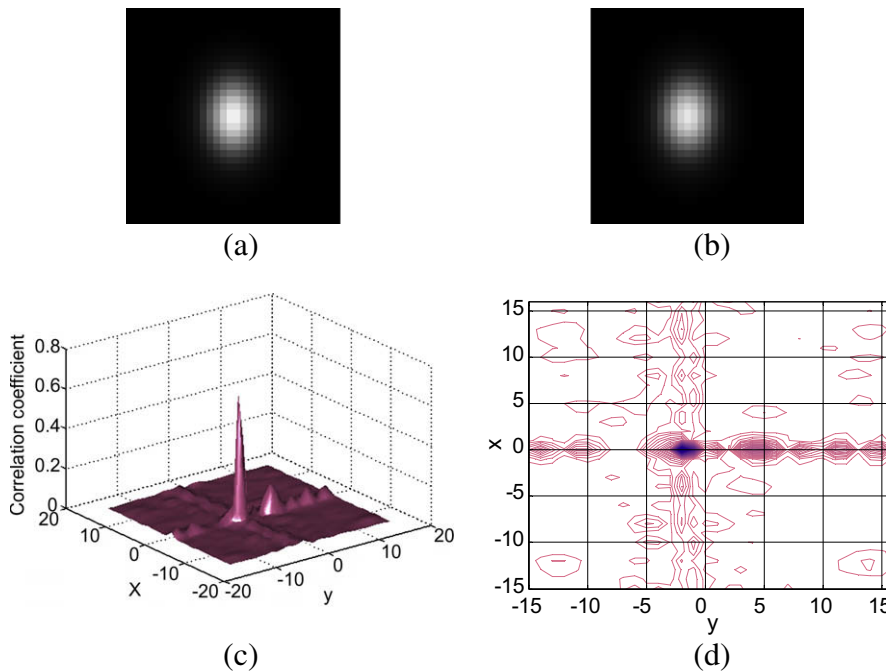
2.4.1. Recovering the rotation matrix

By using the relationship between the Fourier transform magnitudes in Eq. (13), the rotation matrix can be recovered by minimizing the energy

$$E = \int \int \int (\mathfrak{F}[g](W) - \mathfrak{F}[f](RW))^2 dW, \tag{16}$$

and the optimum rotation axis and rotation angle can then be recovered by

$$(\hat{\theta}, \hat{\phi}, \hat{\psi}) = \arg\min_{\theta,\phi,\psi} E. \tag{17}$$

The minimization problem in Eq. (17) can be most efficiently solved by the Quasi-Newton method [22].

2.4.2. Recovering the translation vector

After the rotation estimation, the rotational version of f, Rf, is calculated. Thus, the translation vector can be easily recovered by a phase-correlation technique:

$$\widehat{corr} = \frac{\mathfrak{F}[g](W)\mathfrak{F}*[f](RW)}{|\mathfrak{F}[g](W)||\mathfrak{F}[f](RW)|} = e^{jW^T\cdot t}, \tag{18}$$

where ∗ denotes complex conjugate and g denotes vector dot product. The inverse Fourier transform of the right-hand side of Eq. (18) is the Dirac impulse function. So the translation vector can be found by simply finding the position of that impulse function. According to the rotation and translation estimation, an aligned image from g to f can be denoted as $\tilde{g}$ and $\tilde{f}$, whose spectrum are $\tilde{F}$ and $\tilde{G}$, respectively.

In the Fourier registration process, a 3D window was applied to eliminate the spurious introduction of high-frequency spectral energy due to boundary effects [23]. Experimentally, we found the Blackman window worked best for this dynamic renal data since it makes use of more information in the center of the image. The window size was adapted to voxel resolution and the size of the kidney.

Fig. 4. Illustration of translation effects on phase correlation coefficient plot. A homogeneous 3D image g was generated by translating image f with parameters: [0 −2 0]. Both images have dimensions of [32 32 32]. (a) and (b) are the 16th slice in XY plane of images f and g; (c) is the 16th slice of phase correlation coefficient in XY plane; (d) is the contour plot of figure (c), in which the peak value location is the exact translation estimation between image f and g.

Table 1
Simulated motion for each time frame (T).

T	Motion	T	Motion	T	Motion
1	Baseline	8	LR(−1.66 mm) + (90, 0, 5)	15	HF(3.32 mm)
2	AP(−2.5 mm) + (0, 90, −9)	9	AP(2.5 mm)	16	AP(5.0 mm)
3	LR(3.32 mm) + (90, 0, −2)	10	Baseline	17	Baseline
4	HF(6.64 mm)	11	HF(1.66 mm)	18	HF(−4.98 mm)
5	(0, 0, −4)	12	HF(−1.66 mm)	19	Baseline
6	HF(−6.64 mm)	13	Baseline	20	LR(−4.98 mm)
7	Baseline	14	LR(6.64 mm)		

3. Experiments and results

3.1. Simulated clinical study

The anatomy of the intrarenal regions was constructed based on the in vivo MRR images acquired at 1.5 T (Avanto; Siemens Medical Solutions, Erlangen, Germany) with a T1-weighted 3D gradient echo sequence (TR/TE/FA = 2.84/1.05/12, interpolated matrix $256 \times 256 \times 40$, FOV 425 mm × 425 mm × 100 mm, parallel imaging factor of 3, acquisition time 3 s) and segmented manually into cortex, medulla, and collecting system by an experienced radiologist.

Based on a manually registered 4D MR renography data set, a simulated data set with dimension $[x, y, z, t] = [77\ 97\ 40\ 20]$ and voxel resolution 1.66 mm × 1.66 mm × 2.5 mm was generated by translating and rotating the kidney. Simulated motions included head-to-feet (HF) translation, left to right (LR) translation, anterior to posterior (AP) translation and rotation (Rot) with respect to three different axes, represented in terms of (θ, ϕ, ψ) (Table 1).

Translation estimation errors with mean value and standard deviation were 0.53 ± 0.47, 0.51 ± 0.46, and 0.60 ± 0.41 in x, y, and z direction, respectively. For rotation, the errors were 0.003 ± 0.003, 0.07 ± 0.26, and 1.14 ± 0.72 degrees for (θ, ϕ, ψ).

3.2. Clinical evaluation

In order to evaluate the performance of our Wavelet Representation and Fourier transformation (WRFT) algorithm clinically, our

algorithm was applied to 12 patient datasets (24 kidneys in total). Our study used 3D manual registration and manual segmentation results from experienced radiologists as ground truth. All datasets consisted of at least 41 3D acquisitions acquired over 20 min. Each 3D dataset was comprised of 40 interpolated partitions of 2.5 mm thickness, with an in-plane matrix of 256 and in-plane voxel size 1.66 × 1.66 mm.

In order to extract time course, after registration, three intrarenal regions, the cortex, medulla, and collecting system, were differentiated by applying manual segmentation labels on the first frame, assuming that the following frames have been correctly registered. The time-intensity curves of cortex, medulla, and collecting systems were calculated both for the manually registered data sets and our automatically registered data sets. As a comparison with an alternative 3D registration method, the time-intensity curves based on mutual information (MI) [24] were also calculated.

In Fig. 5, results from the three registration methods are shown for each kidney region for a sample representative subject. Qualitatively, time-intensity curves based on WRFT registration were much closer to the ground truth than MI derived measures. The root mean squared (RMS) relative errors of time-intensity curves between automatic registration methods, WRFT or MI, and ground truth were calculated and are shown in Fig. 6.

From the box-plot, the relative errors based on our WRFT method were much smaller than the MI methods in terms of average and standard deviation of RMS measurements. The average errors for cortex, medulla, and collecting systems in WRFT method were
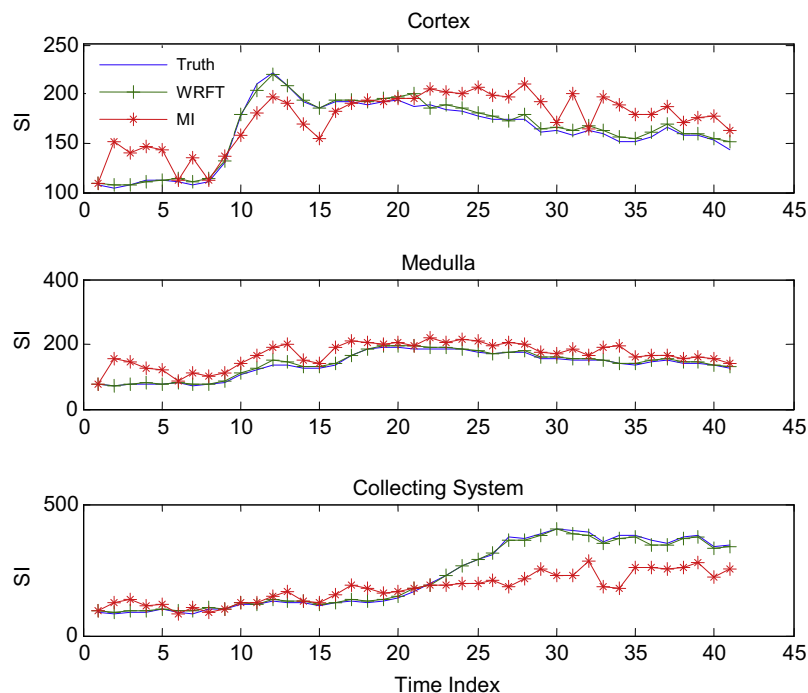

Fig. 5. Average intensity curves for one of the data sets using manual registration, WRFT, and mutual information registration.
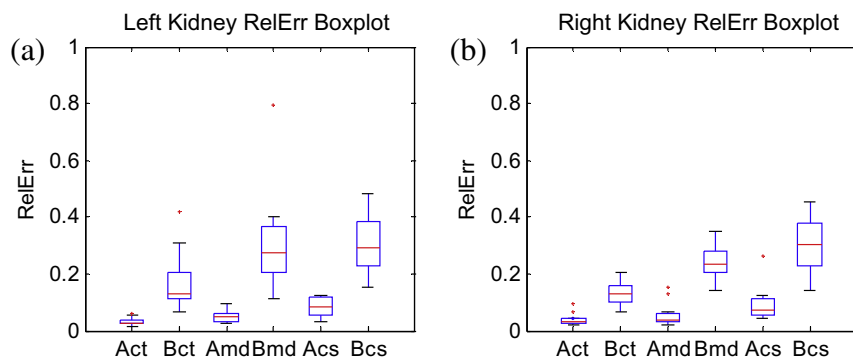
Fig. 6. Boxplot for RMS evaluation of the time-intensity curves generated from WRFT (A) and MI (B) methods. 'ct' stands for cortex; 'md' stands for medulla; 'cs' stands for collecting system. (a) left kidneys, (b) right kidneys.

$3.24\% \pm 1.41\%$, $5.31\% \pm 2.19\%$, and $8.23\% \pm 3.35\%$, respectively, for the left kidney and $3.99\% \pm 2.23\%$, $5.67\% \pm 4.13\%$, and $9.26\% \pm 5.94\%$ for the right kidney.

Evaluation of the statistical differences of results from the two registration methods was performed at the significance level 0.05 with a Wilcoxon signed rank test for paired data. Significance values for the three regions for each pair of registration methods showed small p values (below 0.05), which indicated a significant statistical difference between the methods. According to the box-plot, we can see WRFT had lower mean and smaller standard deviation compared with MI, so WRFT statistically performed better than MI.

The total processing time for the whole WRFT framework was no more than 12 minutes to register each 4D dataset, executing on a Pentium 4 class PC.

4. Conclusions

In 4D (3D plus time) MRI renography, image misalignment due to respiration complicates downstream analysis for computing single kidney glomerular filtration rate and split renal function. Manual correction of such motion for each 4D dataset typically requires approximately 3–4 h at the workstation per case, which is prohibitively time- and labor-intensive for practical clinical use. In this paper, we proposed a novel fully automated four-dimensional MRI renography registration framework which will need 15–20 min based on an over-complete dyadic Wavelet Representation and Fourier Transform (WRFT) method. An edge-preserving anisotropic diffusion operator was also introduced as a denoising method and an optimal edge detection method were compared. The complete method was tested in terms of automation, robustness, and accuracy by both simulated motion and clinical evaluation of patient studies. A comparison between WRFT and mutual information (MI) was implemented to illustrate the effectiveness of the proposed scheme with an alternative existing state-of-art approach. Experimental results showed accurate time-intensity plots resulting from automated registration when compared to data from manually registered images. Executing on a Pentium 4 class PC, it took no more than 12 min to register each 4D dataset. This is about a 10-fold saving in time compared to manual alignments and processing. Furthermore, as a fully automated method, our framework requires no manual involvement or intervention from radiologists. As a complete 4D registration framework, the method may also be applied to additional time-series MRI data, especially other abdominal soft tissue organs, such as lung tumors.

References

[1] V.S. Lee, H. Rusinek, M.E. Noz, P. Lee, M. Raghavan, E.L. Kramer, Dynamic three-dimensional MR renography for the measurement of single kidney function: initial experience, Radiology 227 (2003) 289–294.

[2] S.E. Yuksel, A. El-Baz, A.A. Farag, M.E.A. El-Ghar, T.A. Eldiasty, M.A. Ghoneim, Automatic detection of renal rejection after kidney transplantation, International Congress Series 1281 (2005) 773–778.

[3] J.D. Grattan-Smith, M.R. Perez-Bayfield, R.A. Jones, S. Little, B. Broecker, E.A. Smith, H.C. Scherz, A.J. Kirsch, MR imaging of kidneys functional evaluation using F-15 perfusion imaging, Pediatric Radiology 33 (2003) 293–304.

[4] Y. Sun, J.M.F. Moura, D. Yang, Q. Ye, C. Ho, Kidney segmentation in MRI sequences using temporal dynamics, in: IEEE International Symposium on Biomedical Imaging, 2002, pp. 98–101.

[5] Y. Boykov, V.S. Lee, H. Rusinek, R. Bansal, Segmentation of dynamic N–D data sets via graph cuts using markov models, in: Proceedings of the 4th International Conference on Medical Image Computing and Computer-Assisted Intervention, 2001, pp. 1058–1066.

[6] J.A.d. Priester, A.G. Kessels, E.L. Giele, J.A.d. Boer, M.H. Christiaans, A. Hasman, J.M.v. Engelshoven, MR renography by semiautomated image analysis: performance in renal transplant recipients, Journal of Magnetic Resonance Imaging 14 (2001) 134–140.

[7] Y. Sun, M.-P. Jolly, J.M.F. Moura, Integrated Registration of Dynamic Renal Perfusion MR Images, in: IEEE International Symposium on Image Processing, ICIP'04, Singapore, 2004.

[8] S.N. Gupta, M. Solaiyappan, G.M. Beache, A.E. Arai, T.K.F. Foo, Fast method for correcting image misregistration due to organ motion in time-series MRI data, Magnetic Resonance in Medicine 49 (2003) 506–514.

[9] P.J. Yim, H.B. Marcos, M. McAuliffe, D. McGarry, I. Heaton, Registration of time-series contrast enhanced magnetic resonance images for renography, in: 14th IEEE Symposium Computer-Based Medical Systems, 2001, pp. 516–520.

[10] Y. Sun, J.M.F. Moura, C. Ho, Subpixel registration in renal perfusion MR image sequence, in: IEEE International Symposium on BioImaging, ISBI'04, Crystal City, VA, 2004.

[11] G. Gerig, R. kikinis, W. Kuoni, G.K.v. Schulthess, O. Kubler, Semiautomated ROI analysis in dynamic MRI-studies: Part I: image analysis tools for automatic correction of organ displacement, IEEE Transaction on Image Processing 11 (1992) 221–232.

[12] E.L.W. Giele, J.A. dePriester, J.A. Blom, J.A.d. Boer, J.M.S.v. Engelshoven, A. Hasman, M. Geerlings, Movement correction of the kidney in dynamic MRI scans using FFT phase difference movement detection, Journal of Magnetic Resonance Imaging 14 (2001) 741–749.

[13] J. Montagnat, M. Sermesant, H. Delingette, G. Malandain, N. Ayache, Anisotropic filtering for model-based segmentation of 4D cylindrical echocardiographic images, Pattern Recognition Letters 24 (2003) 815–828.

[14] J. Weickert, B.M.t.H. Romeny, M.A. Viergever, Efficient and reliable schemes for nonlinear diffusion filtering, IEEE Transaction on Image Processing 7 (1998) 398–410.

[15] P. Perona, J. Malik, Scale-space and edge detection using anisotropic diffusion, IEEE Transaction on Pattern Analysis and Machine Intelligence 12 (1990) 629–639.

[16] Q. Duan, E.D. Angelini, A. Laine, Assessment of visual quality and spatial accuracy of fast anisotropic diffusion and scan conversion algorithms for real-time three-dimensional spherical ultrasound, in: Proceedings of SPIE, Medical Imaging 2004: Ultrasonic Imaging and Signal Processing, 2004, pp. 331–342.

[17] J. Weickert, B.M.t.H. Romeny, M.A. Viergever, Efficient and reliable schemes for nonlinear diffusion filtering, IEEE Transactions on Image Processing 7 (1998) 398–410.

[18] Y. Jin, Multi-scale processing of tomographic images using dyadic wavelet expansions, in: Biomedical Engineering, Columbia University, New York, 2004, pp. 1–221.

[19] S. Mallat, A Wavelet Tour of Signal Processing, Academic Press, 1998.

[20] J. Kalifa, A. Laine, P. Esser, Regularization in tomographic reconstruction using thresholding estimators, IEEE Transaction on Medical Imaging 22 (2003) 351–359.

[21] H.S. Stone, B. Tao, M. McGuire, Analysis of image registration noise due to rotationally dependent aliasing, Journal of Visual Communication and Image Representation 14 (2003) 114–135.

[22] D.F. Shanno, Conditioning of quasi-newton methods for function minimization, Mathematics of Computing 24 (1970) 647–656.

[23] H.S. Stone, M.T. Orchard, E.-C. Chang, S.A. Martucci, A fast direct fourier-based algorithm for subpixel registration of images, IEEE Transaction on Geoscience and Remote Sensing 39 (2001) 2235–2243.

[24] ITK. Available from: <http://www.itk.org/>.